PNAS RESEARCH ARTICLE | BIOPHYSICS AND COMPUTATIONAL BIOLOGY ENGINEERING OPEN ACCESS

Acquired motility of *Babesia microti*–infected red blood cells

Chao Li[a], Amy L. Apgar[b], Danielle M. Tufts[c,d], and Tagbo H. R. Niepa[a,b,1]

Edited by David Weitz, Harvard University, Cambridge, MA; received May 28, 2025; accepted December 28, 2025

Babesia microti is an intraerythrocytic protozoan parasite and the main causative agent of human babesiosis in the United States. While extensive research has focused on the prevalence of this vector-borne pathogen in natural populations, increases of human cases and clinical manifestation, and pathogen structure, little is known about the movements of _B. microti_ within vertebrate red blood cells (RBCs). RBCs are nonmotile due to their lack of cellular structures for active movement. Here, we report a phenomenon in which _B. microti_–infected RBCs exhibit an acquired motility compared to uninfected RBCs. Using live-cell tracking, we observed a subset (around 1% in whole blood and 10% in 1:100 diluted blood) of infected RBCs displayed active movement. This acquired motility suggests that _B. microti_ may induce host cell modifications that facilitate its survival, dissemination, or immune evasion potential, allowing it to successfully move through the blood and infect new RBCs. Our findings highlight unconventional RBC dynamics and a potential broad aspect of _B. microti_ pathogenesis. Further investigation into the molecular mechanisms underlying this phenomenon could provide insights into parasite–host interactions and reveal targets for therapeutic intervention in treatment and/or prevention of babesiosis.

cell motility | *Babesia microti* | RBC | whole blood | mitochondrial activity

Significance

This study reveals a phenomenon where *Babesia microti*–infected red blood cells (RBCs), traditionally thought to be nonmotile, exhibit an acquired motility, likely from the movements of the intracellular parasite. Through live-cell tracking, we observed that a subset of infected RBCs can actively move at a velocity up to 5 μm/min (comparable to the typical velocity of macrophages, 1 to 3 μm/min). This acquired motility suggests that *B. microti* may induce host cell modifications that aid its survival, dissemination, or immune evasion. Our findings provide insights into RBC and parasite dynamics, offering a foundation for exploring how these behaviors influence disease progression.

Protozoan parasites, such as *Babesia microti*, are significant causative agents of infectious diseases, posing serious health threats worldwide (1). *Babesia* is a genus of piroplasm parasites belonging to the phylum Apicomplexa, known for infecting RBCs (erythrocytes) in a variety of vertebrate hosts, including humans (2). It is primarily transmitted by Ixodid ticks, notably *Ixodes scapularis*, which also vectors *Borrelia burgdorferi*, a causative agent of Lyme disease. *Babesia microti* is the most common species infecting humans in the United States (3), although others such as *Babesia divergens* and *Babesia duncani* are also clinically significant in Europe and the Pacific Northwest (4, 5), respectively. Research on *Babesia* has intensified due to the parasite's growing public health relevance, especially in immunocompromised patients (6) and through vertical transmission (7–11) and transfusion-transmitted infections (4).

Biologically, *Babesia* has a complex life cycle involving both asexual replication in vertebrate RBCs and sexual stages within the tick vector (12). Once transmitted via tick bite, sporozoites enter the bloodstream and invade erythrocytes, where they differentiate into trophozoites and undergo binary fission (merogony) to produce merozoites (i.e., free *B. microti* cells released into plasma from infected RBCs). The merozoites exit the RBC and can invade new RBCs, perpetuating the infection (12). The mechanisms of erythrocyte invasion are still being elucidated (13, 14), but *Babesia* uses a set of secreted proteins from organelles such as micronemes (15) and rhoptries (16)—similar to *Plasmodium*—to attach and enter host cells.

Understanding the motility of *Babesia* is crucial, as movement plays a vital role in their life cycle (17), host invasion (18), and pathogenesis (19). Motility mechanisms enable the parasite to navigate through host tissues (20), evade immune responses (21), and establish infections (22). In *B. microti*, movement facilitates RBC invasion (23), a key step in disease progression. Studying these motility processes can provide insights into parasite biology, reveal potential drug targets, and aid in developing novel intervention strategies to combat protozoan infections more effectively (24). Recent studies have advanced our understanding of *B. microti* motility, particularly in relation to its invasion of host erythrocytes. Proteomic analyses have identified key proteins involved in intracellular signaling, cytoskeletal support, and protein transport, which are essential for the parasite's movement and host cell invasion (25). Additionally, research into the thrombospondin-related anonymous protein (TRAP) superfamily has highlighted their role in motility and host cell invasion, suggesting that these proteins could be potential targets for therapeutic interventions (26).

Author affiliations: [a]Department of Chemical Engineering, Carnegie Mellon University, Pittsburgh, PA 15213; [b]Department of Biomedical Engineering, Carnegie Mellon University, Pittsburgh, PA 15213; [c]Department of Infectious Diseases and Microbiology, School of Public Health, University of Pittsburgh, Pittsburgh, PA 15261; and [d]Department of Veterinary Tropical Diseases, University of Pretoria, Pretoria 0110, South Africa

Author contributions: C.L., A.L.A., D.M.T., and T.H.R.N. designed research; C.L. and A.L.A. performed research; C.L., D.M.T., and T.H.R.N. contributed new reagents/analytic tools; C.L., A.L.A., D.M.T., and T.H.R.N. analyzed data; and C.L., A.L.A., D.M.T., and T.H.R.N. wrote the paper.

The authors declare no competing interest.

This article is a PNAS Direct Submission.

[1]To whom correspondence may be addressed. Email: tniepa@andrew.cmu.edu.

This article contains supporting information online at https://www.pnas.org/lookup/suppl/doi:10.1073/pnas.2509776123/-/DCSupplemental.

Published February 2, 2026.

Recently, we developed a whole blood cell functional assay platform known as "μ-Blood" (Fig. 1 *A* and *B*) (27) and validated its utility using *B. microti*–infected RBCs (28). On μ-Blood, unprocessed whole blood can be readily distributed to a microchannel [e.g., 0.5 mm in length (*L*) and 0.1 mm in width (*W*) connecting two circular spots 2 mm in diameter, written as 2-2-*L*0.5-*W*0.1] under oil (Fig. 1*C*), forming a quasi-monolayer of blood cells that allows free physical and optical access to the infection in vitro (Fig. 1*D*). Enabled by the unique under-oil assay microenvironment, infection dynamics (i.e., the pathogen behavior over time) can be monitored for days in vitro with the integrity of the original whole blood microenvironment preserved. In this study, we uncovered a phenomenon relating to the acquisition of motility in *B. microti*–infected RBCs in blood from severe combined immunodeficiency (SCID) mice. RBCs are typically nonmotile due to the absence of cellular structures required for active movement. However, we observed that a subset of *B. microti*–infected RBCs exhibited active motility, suggesting a parasite-induced alteration of host cell behavior. This finding raises intriguing questions about the mechanisms driving this movement and its potential biological function in parasite survival, immune evasion, and pathogenesis of *B. microti*.

Results

***Babesia microti* Infection Induces Power Law Motion of Infected RBCs.** We established an infection interface between uninfected blood and *B. microti*–infected blood using the μ-Blood microchannel by loading blood to the designated areas at each end (Fig. 1*C*). The purpose of this experiment was to investigate how *B. microti* propagates from infected RBCs to uninfected RBCs in whole blood. In a 2.5-h timelapse we observed a unique phenomenon with a small subgroup (<1%) of *B. microti*–infected RBCs that demonstrated acquired motility (Fig. 1*E* and Movie S1). RBCs are known to lack the capability of performing active movement. However, the *B. microti*–infected RBC recorded in the timelapse showed a clear directional movement (nearly perpendicular to the microchannel length direction) with a velocity of approximately 2 μm/min, pushing through a dense layer of uninfected RBCs (Fig. 1 *E–H*). The velocity of this acquired motility is comparable to the typical migration velocity of macrophages in vivo at about 1 to 3 μm/min (29).

Visualized by a dye that illuminates live mitochondria (MitoTracker Orange), the timelapse video also recorded the intraerythrocytic motion of the parasite cell during the directional movement of the infected RBC (Fig. 1 *G* and *H*). At the beginning of the event, the RBC infected by a *B. microti* protozoan was located among uninfected RBCs (Fig. 1*E*). The parasite inside the RBC was observed to collide with the RBC membrane at the leading edge, effectively pushing the infected RBC out of the constraint from the uninfected RBC on top (t0-t85, Fig. 1 *F*, *Left*). The continuous momentum from the parasite apparently drives the following directional movement of the infected RBC through the quasi-monolayer of uninfected RBCs (t86-t117, Fig. 1 *F*, *Middle*). At the end, the parasite was observed to egress from the infected RBC (t118-t150, Fig. 1 *F*, *Right*). The mean squared displacement (MSD) analysis (Fig. 1*F* and *Materials and Methods*) revealed that the movement of *B. microti*–infected RBC was in superdiffusive mode with α (the fitting exponent) = 1.4 (RBC constraint evasion), α = 1.7 (RBC directional movement), and α = 1.4 (*B. microti* egress), respectively. After egress, the previously infected RBC remained stationary. These observations indicated that *B. microti* drives the motility of an RBC from inside the cell. To understand this acquired motility and the underlying driving mechanism, we further examined *B. microti* motility inside and outside RBC.

***B. microti* Motility Inside an RBC.** We used the phase-contrast confocal imaging protocol [established in our previous study (28)] to track the motility of *B. microti* in RBCs at varying binary fission stages (Fig. 2). Enabled by the large contrast ratio in phase contrast between RBC cytosol and *B. microti*, the parasite can be easily identified and tracked in RBCs, taking pleomorphic forms including Ring (1 parasite), Paired-Pyriform (2 parasites), Maltese Cross (4 parasites), and multiple parasites (4+ parasites) (*SI Appendix*, Fig. S1). The typical size comparison between RBC and *B. microti* is about 6 to 8 μm (the diameter of RBC when taking the regular biconcave shape) vs. 1 to 2 μm (the diameter of a single *B. microti* cell).

Tracking results showed that *B. microti* can move inside an RBC with a velocity up to 2.9 μm/min (Fig. 2*A* and Movie S2), navigating through a maximum displacement of about 3.3 μm in 18 min (Fig. 2 *B* and *C*). This displacement corresponds to 3.3 μm/[7 μm (RBC diameter)—2 μm (*B. microti* diameter)] × 100% ≈ 70% of the free moving space available inside an RBC (Fig. 2*D*). Quantified by MSD analysis, the intraerythrocytic *B. microti* motion was identified in superdiffusive or power law mode with the average α = 1.4 ± 0.4 (RBC with 1 parasite) (Fig. 2 *B* and *C*), α = 1.9 ± 0.8 (RBC with 2 parasites) (*SI Appendix*, Fig. S1 *B* and *C*), α = 1.9 ± 1.0 (RBC with 4 parasites) (*SI Appendix*, Fig. S1 *E* and *F*), and α = 1.3 ± 0.3 (RBC with 4 + parasites) (*SI Appendix*, Fig. S1 *H* and *I*). The intraerythrocytic velocity of *B. microti* drops significantly by approximately 50% [mean velocity, $P < 0.0001$ (One-way ANOVA)] when the number of parasites increases to four or more parasites in an RBC (*SI Appendix*, Fig. S1*J* and Movie S2). This velocity decrease could be apparently attributed to the decreased free moving space when more parasites are present. There could also be biological factors behind the change of intraerythrocytic velocity of *B. microti*, e.g., possibly related to a specific binary fission stage and/or quorum sensing.

These intraerythrocytic *B. microti* motility tracking results confirmed that the parasite can actively move inside RBCs, providing momentum necessary for propelling the host cell in a direction. It is known that RBCs lack mitochondria, relying on anaerobic glycolysis in the cytosol for energy (30). In comparison, *B. microti* primarily utilizes mitochondrial respiration for energy (31–33). To further understand the acquired motility of *B. microti*–infected RBCs, we investigated the mitochondrial activity in *B. microti* and how *B. microti* motility changes once released into plasma in the form of merozoites.

***B. microti* Motility Outside an RBC.** From the phase contrast channel and the MitoTracker Orange channel combined, four cellular objects in *B. microti* infection were identified on μ-Blood, including *B. microti*–infected RBC, *B. microti* inside RBC, *B. microti* outside RBC (i.e., merozoite), and mitochondrion (Fig. 3). The mitochondrion movement inside *B. microti* can be tracked and quantified from the MitoTracker Orange channel [Fig. 3 *A–D* and Movie S3 (video on left)]. The maximum mitochondrion velocity observed was about 12.2 μm/min, 4 to 6 times the velocity of a *B. microti*–infected RBC (1.5 μm/min) and the velocity of intraerythrocytic *B. microti* (2.9 μm/min), respectively. The mitochondrion movement showed no noticeable connection to the number of parasites in an RBC, which is distinctive from intraerythrocytic *B. microti* motility (Fig. 2 and *SI Appendix*, Fig. S1). Quantified by MSD analysis, the mitochondrion movements were identified in ballistic mode with the average α = 2.3 ± 2.2. These results revealed that mitochondria are very active in live *B. microti* cells, producing energy (34) for the parasite metabolism and motility.

Using the same tracking method, *B. microti* merozoites—free parasites released into plasma after egress from an RBC—can also be identified by phase contrast and further confirmed by the positive MitoTracker Orange signal. Once released into plasma, *B. microti* merozoites showed a significantly [$P < 0.0001$ (t test, one-tail)] increased maximum velocity around 38.8 μm/min [Fig. 3 *E–H* and Movie S3 (video on right)]—around 13 times the maximum velocity of intraerythrocytic *B. microti* (2.9 μm/min). In high velocity compared to the intraerythrocytic *B. microti* motility, the merozoite movements were identified in power law mode with the average $\alpha = 1.5 \pm 0.7$.

These motion tracking results (Fig. 3) confirmed 1) *B. microti* moves inside an RBC in superdiffusive or power law mode with a velocity up to 2.9 μm/min; 2) after egress from an RBC and released into the plasma, *B. microti* motility is significantly increased with a velocity up to 38.8 μm/min and with the movements in power law mode; and 3) mitochondria actively move inside live parasites with a velocity up to 12.2 μm/min and with the movements in ballistic mode. Apparently, the movement of *B. microti* inside an RBC fueled by mitochondrial respiration provides the source of propulsion momentum that drives the directional movement of the infected RBC.

Motility of *B. microti*–Infected RBCs in Diluted Blood. We designed an experiment to further validate that the acquired motility of *B. microti*–infected RBCs originates from the parasite inside an RBC rather than passively from other blood cells or fluid in the environment. In this experiment, we diluted *B. microti*–infected whole blood (>80% parasitemia) with Mg^{2+} and Ca^{2+} double-negative phosphate-buffered saline (PBS) (as Ca^{2+} or nutrition can significantly affect cell activity) in a 1:100 volume ratio to get a monolayer of blood cells on the surface in a density lower than fully packed (Fig. 4*A*). With the low cell density in diluted blood, we can reliably rule out the direct cell-to-cell interaction from the other cells and thus the possibility of momentum transfer that may trigger passive movement of the *B. microi*–infected RBCs. We incubated the PBS-diluted blood cells for 2 d to reach a condition that included RBCs with initial hemoglobin, RBCs with low hemoglobin, and RBCs undergoing hemoglobin reduction (Fig. 4 *B* and *C*). Hemoglobin reduction is a process of sudden hemoglobin loss in a process ≤5 min observed in *B. microti*–infected RBCs (28). In addition, the 2-d incubation also led to a stable fluidic environment with little/no flow on the cells that may cause passive cell movement.

We performed a 10-h timelapse (5 min interval) to track the motion of all types of the RBCs (Type 1—nonmotile RBCs undergoing hemoglobin reduction, Type 2—nonmotile RBCs with initial hemoglobin, Type 3—nonmotile RBCs with low hemoglobin, and Type 4—motile RBCs) (Fig. 4 *D–K* and Movie S4). Recorded in the timelapse, a subset of infected RBCs (~10%, Fig. 4*B*) in the PBS solution showed acquired motility with a velocity up to 4.6 μm/min (Fig. 4 *D*, *E*, *H*, and *I*). Compared to the velocity of *B. microti*–infected RBCs recorded in whole blood (~2 μm/min, Fig. 1*G*), the increased motility could be attributed to lower resistance associated with the reduced fluid viscosity (whole blood 3-5 centipoise (cP) at a shear rate of 100/s vs. PBS ~1 cP) and cell density (35). Biochemical factors (e.g., nutrient level, signaling molecules) may also play a role in the change of motility from blood dilution.

The maximum velocity of the infected RBC with low hemoglobin (4.6 μm/min, Fig. 4*E*) was significantly higher [$P = 0.00015$ (t test, one-tail)] than the infected RBC with initial hemoglobin (3.9 μm/min, Fig. 4*I*). We anticipated that the hemoglobin reduction observed in *B. microti*–infected RBCs could be connected to hemoglobin loss triggered by perforation of the RBC cytoplasmic membrane (36). After a significant loss of the hemoglobin content, the mechanical property (e.g., deformability) of the infected RBCs may be altered. MSD analysis on the movements of *B. microti*–infected RBCs (Fig. 4 *F*, *G*, *J*, and *K*) identified the motion type in ballistic mode (i.e., $\alpha > 2$) on average with segment α up to around 10 (Fig. 4 *G* and *K* and *SI Appendix*, Table S1). These MSD results suggested that the acquired motility of *B. microti*–infected RBCs is in active migration rather than passive diffusion driven by the surrounding cells or fluid environment.

RBC morphology (infected vs. uninfected) was characterized using confocal microscopy, transmitting electron microscopy (TEM), and scanning electron microscopy (SEM) (Fig. 5). From the three-dimensional (3D) confocal images with PKH67 cytoplasmic membrane stain, *B. microti* cell(s) can be identified inside infected RBCs (Fig. 5 *A–D*). Compared to uninfected RBCs, the infected RBCs showed significantly deformed cell morphology (Fig. 5 *B* and *D*). The deformed cell morphology of *B. microti*–infected RBCs was further confirmed by TEM images (Fig. 5 *E* and *G*). Further, SEM images revealed that the cytoplasmic membrane of *B. microti*–infected RBCs (Fig. 5 *F* and *H*) was decorated with nanopore structures (about 50 nm in diameter) and in significantly higher frequency (8.6 ± 11.2 pores/RBC) compared to uninfected RBCs (1.1 ± 2.0 pores/RBC) (Fig. 5*I* and *SI Appendix*, Fig. S2). While the nanopores could be generated during SEM sample preparation (specifically cell dehydration), the significantly higher frequency of nanopores on infected RBCs indicated a possible connection of RBC cytoplasmic membrane compromise associated with the intraerythrocytic parasites. Hemoglobin concentration was measured using the Cayman's Hemoglobin Colorimetric Assay Kit (*SI Appendix*, Fig. S3*A*) which revealed higher hemoglobin concentration in infected RBC samples compared to control uninfected RBC samples. The Cayman Assay utilizes a detection agent which is impermeable to an RBC membrane, signifying that an increased concentration of hemoglobin in infected RBC samples could be due to compromised cytoplasmic membrane integrity enabling the release of hemoglobin into the extracellular space. Compromised membrane integrity was further characterized with confocal imaging on infected and uninfected PKH67-stained RBCs 24 h after collection. In uninfected samples, there is variability in high and low hemoglobin content RBCs, and both high and low hemoglobin RBCs retain an in-tact PKH67-stained cytoplasmic membrane (*SI Appendix*, Fig. S3*B*). In infected samples, there is also variability in high and low hemoglobin content RBCs, but low hemoglobin RBCs have weakened and patchy PHK67 cytoplasmic membrane stain retention and the RBCs can become deformed and have less volume (*SI Appendix*, Fig. S3 *C* and *D*). Together, these comparative characterizations on RBC morphology showed that *B. microti* causes significant RBC deformation while maintaining a relatively integrated (i.e., partially compromised) RBC cytoplasmic membrane structure.

To further understand the driving mechanism of the acquired motility of *B. microti*–infected RBCs, we tracked and analyzed the deformation of the motile infected RBCs during their movement (Fig. 6). The results showed that the parasite(s) inside an RBC can deform the host cell up to 20% based on circularity analysis (Fig. 6 *A–C*), which could contribute to the driving force of acquired motility of the infected RBC. Furthermore, the infected RBC with initial hemoglobin showed milder *B. microti*-directed RBC deformation (<10%, Fig. 6 *D–F*) compared to the deformation of infected RBC with low hemoglobin (~20%, Fig. 6*C*). At the later stage, after hemoglobin reduction of the infected RBC, the RBC acquired a noticeably higher deformation (~16%, Fig. 6*F*). These results revealed that the level of hemoglobin content in RBC cytosol may affect the RBC

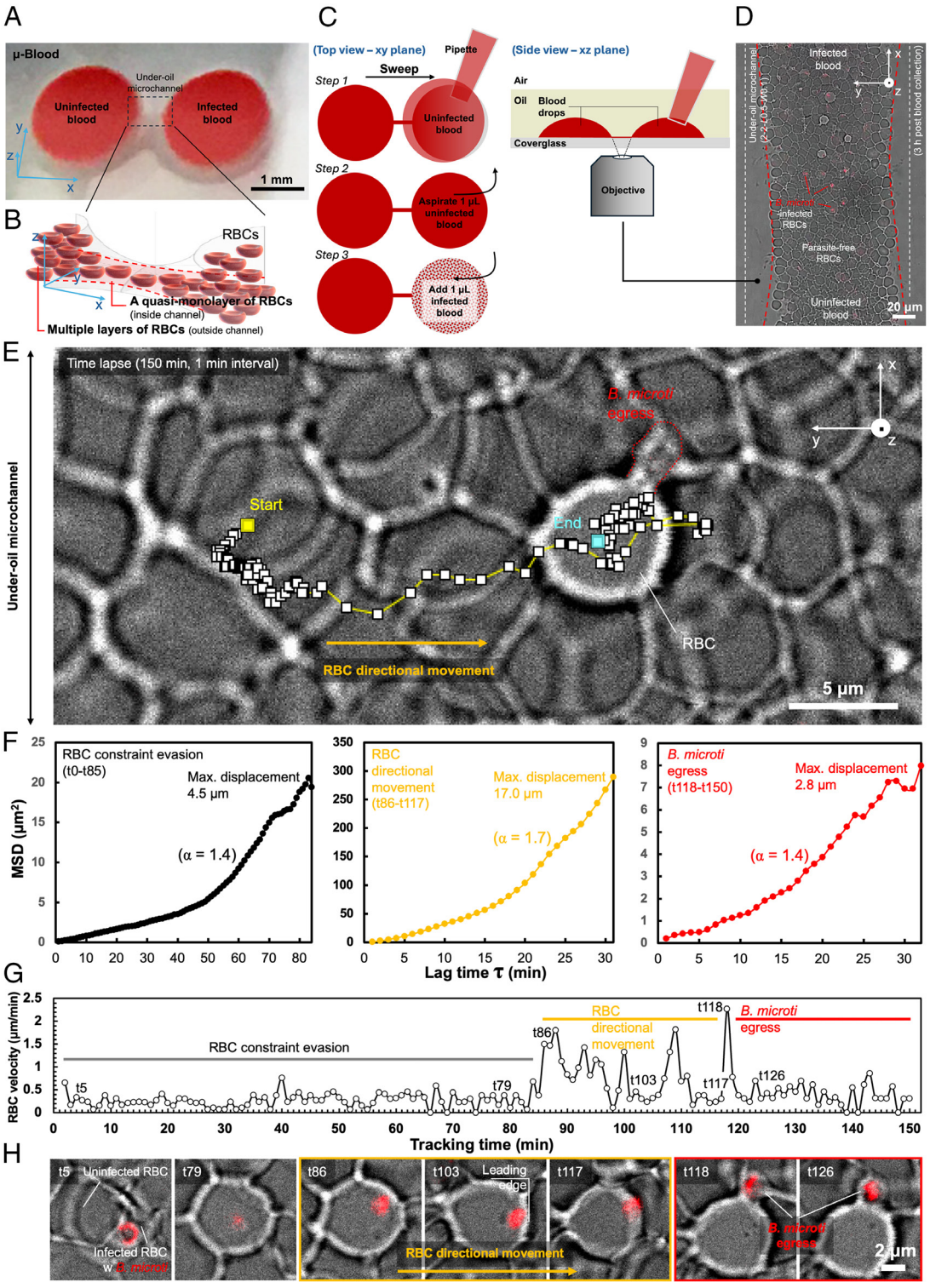

Fig. 1. Directional movement of *B. microti*–infected RBC recorded ex vivo on μ-Blood. (*A*) Image showing an under-oil microchannel (2-2-*L*0.5-*W*0.1) filled with whole blood (28). (*B*) Schematic showing the 3D geometry of the microchannel and the quasi-monolayer of RBCs (denoted by the red dashed lines) spontaneously formed in the microchannel. (*C*) Workflow of blood loading (*Top* view, *Steps* 1, 2, and 3) that generates an infection interface in the microchannel. The side view shows the under-oil microchannel configuration that enables free physical access and uncompromised optical access. (*D*) A microscopic image [phase + MitoTracker Orange, 8-bit, objective—63× (oil immersion)] showing the quasi-monolayer of RBCs. The orientation of the microchannel (white dashed lines) on the microscopic image is rotated 90° counterclockwise (with infected blood on top and uninfected blood at bottom) compared to the μ-Blood device. (*E*) Tracking trajectory of the directional movement of a *B. microti*–infected RBC propelled by the parasite cell from inside. The double-ended arrow on the left of the image shows the direction of the under-oil microchannel. (*F*) MSD analysis of the motility tracking in (*E*) divided into three subtrajectories including (*Left*) RBC constraint evasion (i.e., the escape of the target *B. microti*–infected RBC from underneath an infected RBC on top, t0-t85), (*Middle*) RBC directional movement (t86-t117), and (*Right*) *B. microti* egress (t118-t150). The fitting exponent (α) was calculated with (log) linear regression, averaging the monotonic (i.e., continuously increasing or decreasing) MSD segments in a trajectory. Motion regimes: elastic, $0 \le \alpha < 0.5$; subdiffusive, $0.5 \le \alpha < 1$; normal diffusive (i.e., Brownian motion), $\alpha = 1$; superdiffusive, $1 < \alpha < 1.5$; power law, $1.5 \le \alpha < 2$, and ballistic, $\alpha > 2$. (*G*) Change of RBC velocity over time including RBC constraint evasion (at low velocity <0.5 μm/min), RBC directional movement (at high velocity about 1.5 μm/min), and *B. microti* egress from the infected RBC (instantly propelling the RBC velocity up to 2 μm/min). (*H*) Representative time stamps showing the relative position of the parasite cell (MitoTracker Orange, red fluorescence) inside the infected RBC.

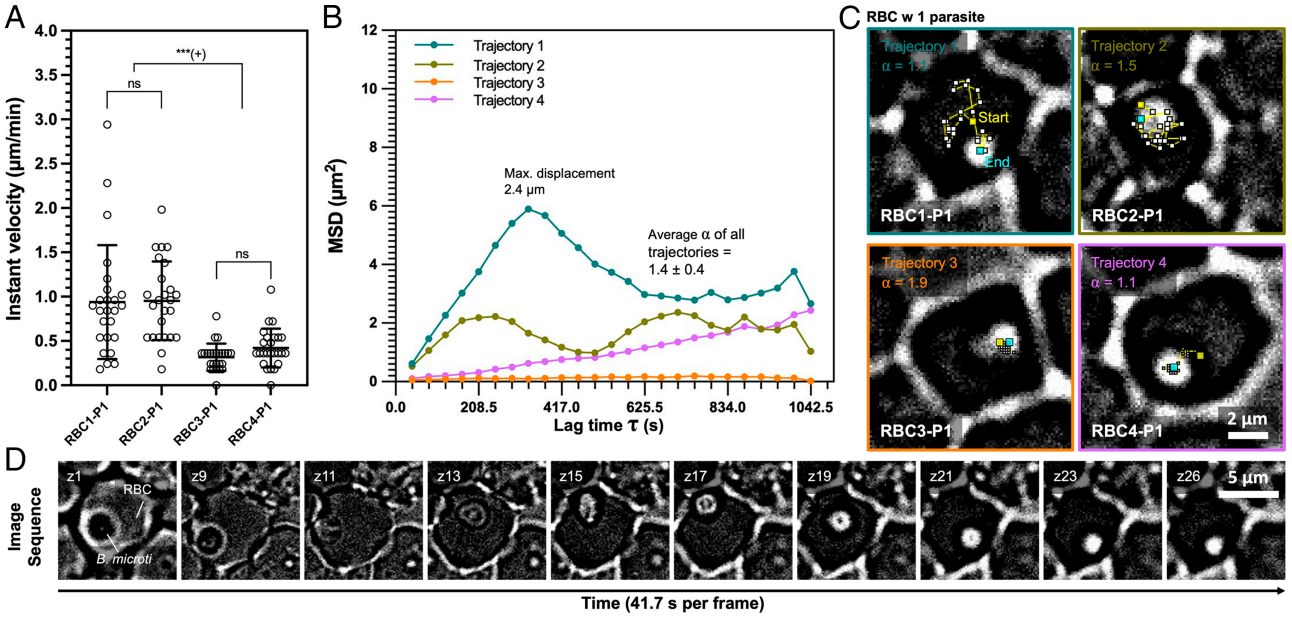

Fig. 2. Label-free motility tracking of *B. microti* movement inside RBC. (*A*) Instant velocity of *B. microti* in an RBC. Each data point on the velocity graph represents the quasi-instant velocity measured between two adjacent frames [z(i) and z(i + 1)] in a tracking trajectory. Error bars, mean ± SD. A one-way ANOVA for multiple comparisons was used to calculate the *P*-values followed by a post hoc Student's *t* test. ***$P \le 0.001$ and ns—not significant. (*B*) MSD analysis of four infected RBCs with one parasite inside (trajectory 1 to trajectory 4). Average α of all trajectories (1.4 ± 0.4) indicates superdiffusive mode. (*C*) Trajectories of the four infected RBCs with one parasite in each RBC (written as RBC1-P1, RBC2-P1, etc.). Motility tracking was executed manually with the apparent geometric center of the object through a z-stack timelapse (26 slices, 41.7 s per frame, the total time of scan—18 min). The tracking trajectory was illustrated in the image with white square dots connected by yellow lines. The yellow and cyan square dots on the trajectories highlight the start and end point, respectively. (*D*) Image sequence showing the position change of a *B. microti* cell inside an infected RBC (RBC1-P1).

deformability apparently driven by the parasite from inside. The molecular mechanisms regarding RBC deformation and the transfer of momentum from the parasite to the movement of RBC require further investigation.

From the same 10-h timelapse, we further monitored and analyzed the mitochondrial activity across the identified cellular objects and during RBC movement (Fig. 6*G*). The results showed that the nonmotile infected RBCs with initial or low hemoglobin can have both high and low mitochondrial activity, probed by MitoTracker Orange intensity. By contrast, the motile infected RBCs with acquired motility all showed high mitochondrial activity, indicating an active energy generation via mitochondrial respiration. These mitochondrial activity results indicated that the acquired motility of *B. microti*–infected RBCs might rely on energy generation from the mitochondria.

Finally, we tracked neutrophil migration in *B. microti*–infected blood on μ-Blood (*SI Appendix*, Fig. S4 and Movie S5) to clarify the difference in motility between neutrophils and *B. microti*–infected RBCs. First, neutrophils are about 10 μm in diameter (slightly bigger than RBCs) when not active. However, when migrating they are significantly [$P < 0.0001$ (*t* test, one-tail)] larger in cell size and morphology (*SI Appendix*, Fig. S4 *A*, *F*, and *G*) compared to motile *B. microti*–infected RBCs (Fig. 6 *A*, *B*, *D*, and *E*). Neutrophils become polarized and elongated with a cell body size measured 10 to 25 μm from the leading edge to uropod [*SI Appendix*, Fig. S4 *A* (*Inset*) and *SI Appendix*, Fig. S4*G*] and able to deform the cell body up to more than a hundred micrometers if exposed to a highly confined space (37). By contrast, the deformation (16 to 18%) of *B. microti*–infected RBCs (Fig. 6 *C* and *F*) is significantly smaller [$P < 0.0001$ (*t* test, one-tail)] compared to neutrophil deformation (average 144%) (*SI Appendix*, Fig. S4 *F* and *G*). Additionally, neutrophils, as the fastest immune cells in the body, can migrate at a velocity around 20 to 30 μm/min. The maximum velocity of neutrophil migration through the quasi-monolayer of RBCs recorded on μ-Blood was 23.1 μm/min (*SI Appendix*, Fig. S4*B*), significantly higher [$P < 0.0001$ (*t* test, one-tail)] than the maximum velocity of *B. microti*–infected RBCs at ~5 μm/min in diluted blood (Fig. 4 *E* and *I*) and at ~2 μm/min in whole blood (Fig. 1*G*). These comparisons ruled out the possibility of the motile cells displayed in Figs. 1, 4, and 6 being neutrophils known to exist in the SCID mouse blood (*SI Appendix*, Fig. S4 and Table S2). SCID mice have a genetic defect that affects the development of B and T lymphocytes (adaptive immune system), but their innate immune system (neutrophils, macrophages, NK cells, etc.) remains functional. We assumed these cells discussed above were neutrophils based on cell morphology (e.g., multilobed nucleus, granules) and the motility results [neutrophils migrate much faster than macrophages (average about 1 to 3 μm/min)] (29) shown in *SI Appendix*, Fig. S4 and Table S2 (38).

Discussion

Distinct from most of the protozoan parasites in the Apicomplexa phylum, *Babesia* spp. (e.g., *B. microti*, *B. divergens*, *B. duncani*, *B. bovis*) exploit host life cycles for variable lengths of time in each life cycle without showing a clear line on maturation depending on the stress the parasites are exposed to, which allows them to gain survival advantage in varying environments (1). Specifically, *B. microti* is difficult to cultivate in vitro once extracted from the host system, resulting in studies heavily relying on lab animals (e.g., mouse models). The unconventional life cycle and poor in vitro culturability leave *B. microti* pathogenesis still largely understudied. The canonical knowledge of the parasite postulates that *B. microti* propagates via egress from infected RBCs followed by reinfection of fresh RBCs (12). Due to limited in situ optical (i.e., microscopic imaging) access to the host (e.g., mice, humans) system, the *B. microti* propagation dynamics is underexplored.

Enabled by μ-Blood, we can directly investigate *B. microti*–infected blood samples in vitro with expanded time (days) and preserved whole blood microenvironment. This allows us to

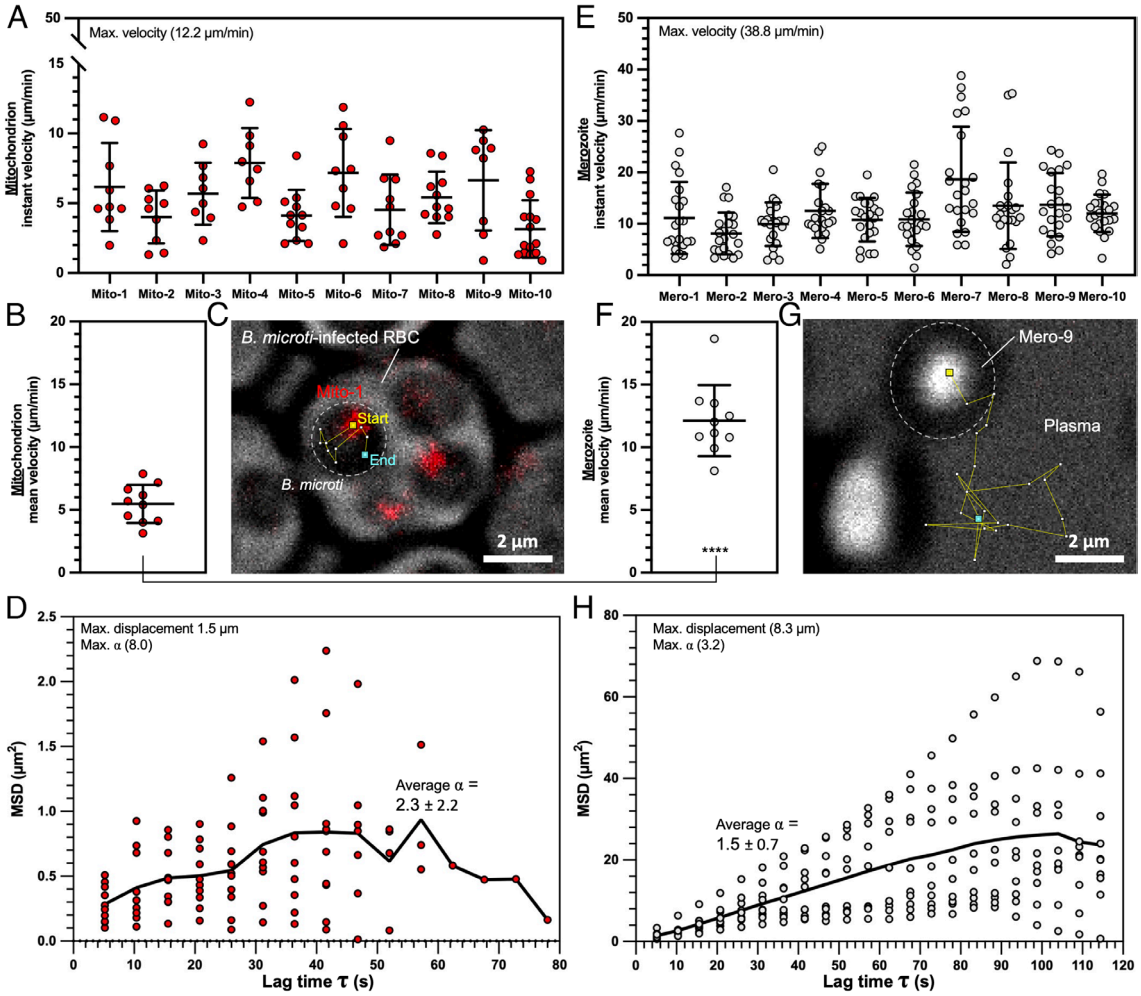

Fig. 3. Motility analysis of parasite mitochondria and free parasite cells released into plasma in B. microti infection. (*A*) Mitochondrion instant velocity in *B. microti* cell. Each data point on the velocity graph represents the quasi-instant velocity measured between two adjacent frames [z(i) and z(i + 1)] in a tracking trajectory. (*B*) Mitochondrion mean velocity. Each data point on the velocity graph represents the mean velocity of a mitochondrion. (*C*) Representative trajectory of mitochondrion (Mito-1). The motility tracking was executed with the apparent geometric center of the object through a z-stack timelapse (23 slices, 5.2 s per frame, the total time of scan—2 min). The tracking trajectory was illustrated in the image with white square dots connected by yellow lines. The yellow and cyan square dots on the trajectories highlight the start and end point, respectively. (*D*) MSD analysis showing the average and maximum α of the ten trajectories. (*E*–*H*) show the results of *B. microti* merozoite motility in plasma. Error bars, mean ± SD. A paired two-tailed *t* test was used to calculate the *P*-value. ****$P \leq 0.0001$.

continuously monitor *B. microti* propagation dynamics with the original in vivo infection factors and uncompromised optical access from both label-free phase contrast and fluorescence tagging. On μ-Blood, we recorded a subgroup of *B. microti*–infected RBCs acquiring motility, apparently from the parasite inside the host cell. This observation challenges our conventional understanding of *B. microti* propagation and reveals a mechanism for the parasite to navigate through its infection niche.

In this study, we analyzed and quantified the motility of all cellular objects identified in *B. microti* infection including (from small to large) *B. microti* mitochondria, intraerythrocytic *B. microti*, free *B. microti* in plasma (i.e., merozoites), *B. microti*–infected RBCs (initial hemoglobin vs. low hemoglobin), and neutrophils. The results revealed and confirmed that mitochondria and the parasite cells are actively moving inside and outside an RBC during the infection and reinfection processes. The active parasite cell movements apparently fuel the acquired motility of a subset (~10%) of infected RBCs, being able to navigate through blood cells in whole blood microenvironments in superdiffusive (or higher) mode at a velocity of 2 to 5 μm/min comparable to host immune cells. These in vitro motility data obtained on μ-Blood (*SI Appendix*, Table S2) provide reference for in vivo study and further confirmation of the acquired motility of *B. microti*–infected RBCs.

This study is limited to biophysics, lacking molecular mechanisms on how the parasite interacts with the host cell structure from inside and how the parasite–host cell interaction transfers the momentum from the parasite to the directional movement of the host cell. The acquired motility of *B. microti*–infected RBCs may benefit the parasites by identifying fresh RBCs in their vicinity without egress from the infected host cell, increasing the chance of immune evasion and energy fitness. Proteome and lipidome studies of the RBC cytoplasmic membrane will help pinpoint the functional molecules that determine the observed acquired motility. RBC motility-related molecules could be potential antiparasitic treatment targets that compromise parasite virulence, therefore sensitizing the infected RBCs to host immune control and clearance. Confirmation of the biological functions of the acquired motility of *B. microti*–infected RBCs requires nutrient constraint and/or host immune challenges (with T cells and NK cells) that are known as the main host control of *B. microti* infection.

This insight into the acquired motility of infected RBCs suggests an additional layer to the canonical *B. microti* propagation sequence, including i) the initial sporozoite infection of RBCs, ii)

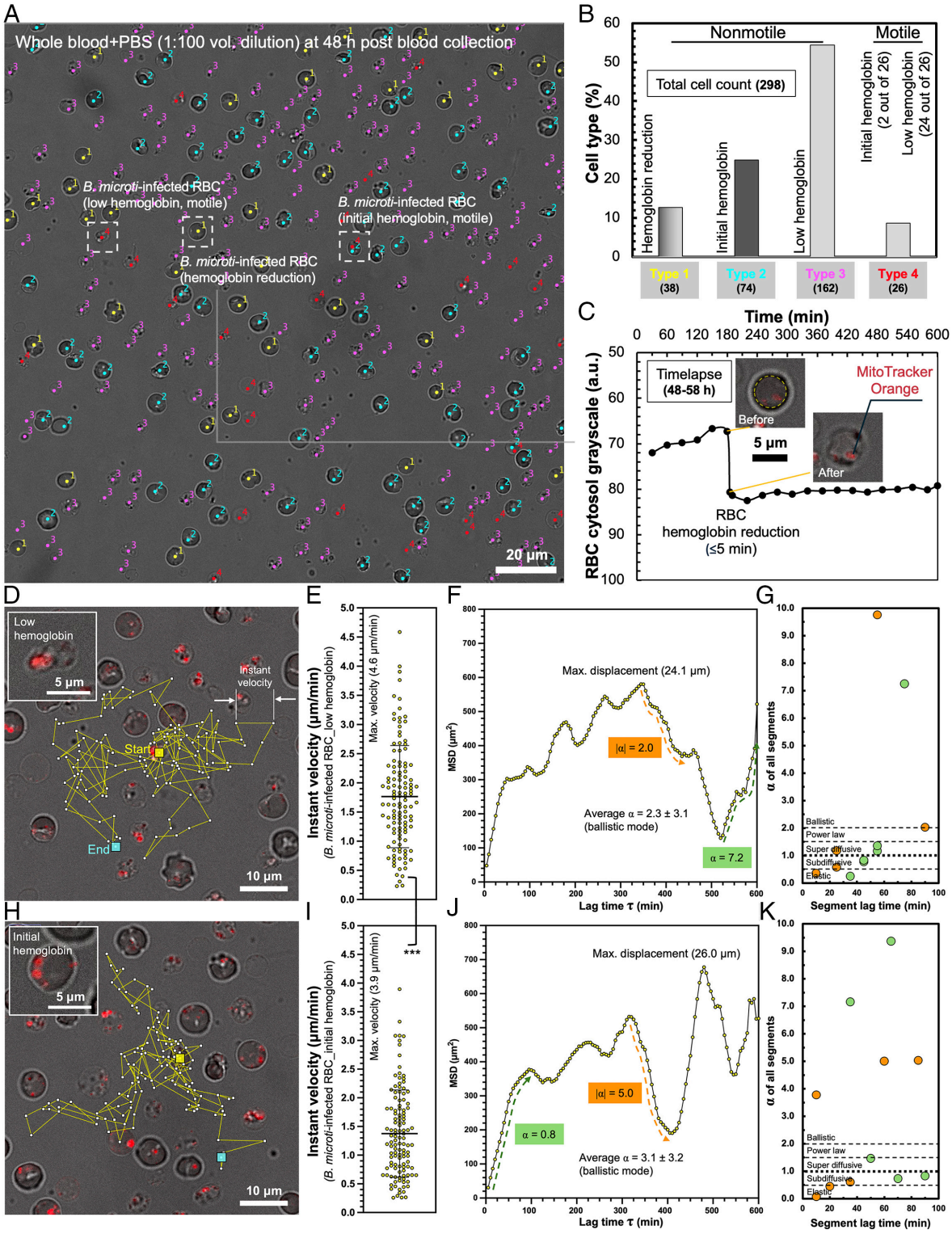

Fig. 4. Motion of *B. microti*–infected RBCs in diluted blood. (*A*) Microscopic image [phase contrast, the first frame in the 10-h (i.e., from 48 to 58 h) timelapse sequence in (*C*)] showing the *B. microti*–infected blood diluted with PBS (1:100 volume ratio) at 48 h post blood collection. (*B*) The four types of blood cells identified in (*A*) include Type 1—nonmotile RBCs undergoing hemoglobin reduction during the timelapse, Type 2—nonmotile RBCs with initial hemoglobin through the timelapse, Type 3—nonmotile RBCs with low hemoglobin since the start of the timelapse, and Type 4—motile RBCs with low or initial hemoglobin. (*C*) Representative RBC hemoglobin reduction process recorded in the 10-h timelapse (5 min interval). (*Insets*) Microscopic images (phase contrast + MitoTracker Orange) showing the difference of RBC cytosol grayscale before and after hemoglobin reduction. The grayscale analysis reflects the hemoglobin content within the RBC cytoplasm. (*D*) Representative tracking trajectory of a motile infected RBC with low hemoglobin. The motility tracking was executed with the apparent geometric center of the object through a timelapse (5 min per frame, the total time of scan—10 h). The tracking trajectory was illustrated in the image with white square dots connected by yellow lines. The yellow and cyan square dots on the trajectories highlight the start and end point, respectively. (*E*) Instant velocity of motile *B. microti*–infected RBCs with low hemoglobin. (*F*) MSD plot of the motility tracking in (*D*). The green dashed-line arrow indicates the dominant trend in the group of increasing segments. The orange dashed-line arrow indicates the dominant trend in the group of decreasing segments. (*G*) α-segment lag time plot showing the distribution of α (increasing segments in green dots, decreasing segments in orange dots) and motion continuity (segment lag time = τ_End - τ_Start of each segment, *SI Appendix*, Table S1). The dashed lines indicate the motion regime boundaries. (*H*–*K*) show the tracking results of *B. microti*–infected RBCs with initial hemoglobin. Error bars, mean ± SD. A paired two-tailed *t* test was used to calculate the *P*-value. ****P* ≤ 0.001.

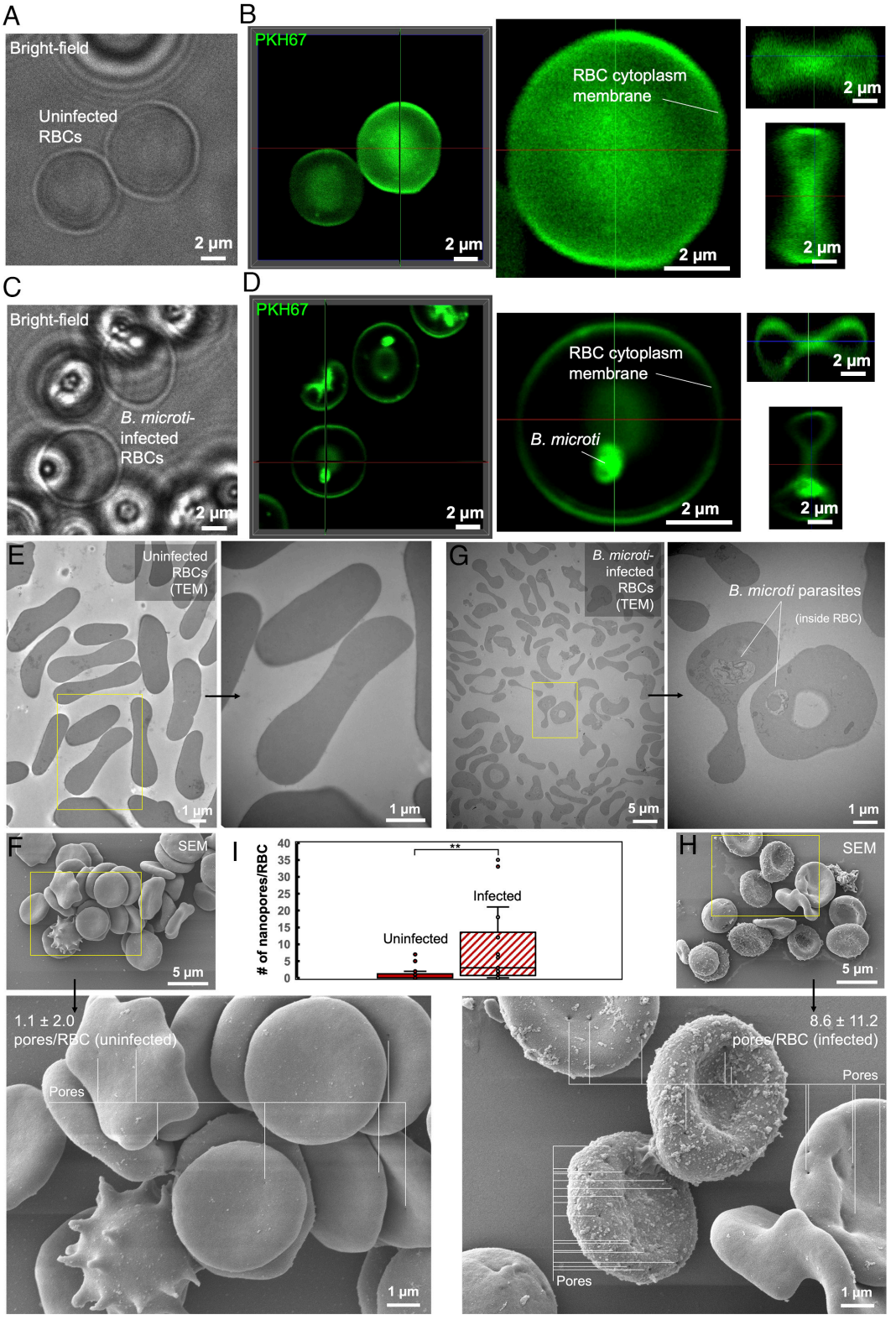

Fig. 5. Morphological change and comparison between uninfected and infected RBCs. (*A*) Bright-field and (*B*) fluorescence confocal images (with 3D view) of PKH67-stained uninfected RBCs. (*C*) Bright-field and (*D*) fluorescence confocal images (with 3D view) of PKH67-stained *B. microti*–infected RBCs. The cytoplasmic membrane of the parasite cell(s) inside RBC was also stained by PKH67. (*E*) TEM and (*F*) SEM images of uninfected RBCs. (*G*) TEM and (*H*) SEM images of *B. microti*–infected RBCs. (*I*) Nanopore distribution on the RBC surface. Nanopores were observed on the cytoplasmic membrane of the SEM RBC samples and significantly more frequent on the *B. microti*–infected RBCs (average 8.6 pores/RBC) compared to uninfected RBCs (average 1.1 pores/RBC) (*SI Appendix*, Fig. S2). Error bars, mean ± SD. A paired two-tailed *t* test was used to calculate the *P*-value. $^{**}P \leq 0.01$.

egress from an infected RBC, iii) migration of a merozoite in plasma, and iv) reinfection of fresh RBCs. Infected RBCs can reposition within the infection niche prior to parasite egress, indicating that parasite movement may occur not only through free merozoite migration but also through host-cell–mediated transport. This acquired motility suggests that parasite relocation

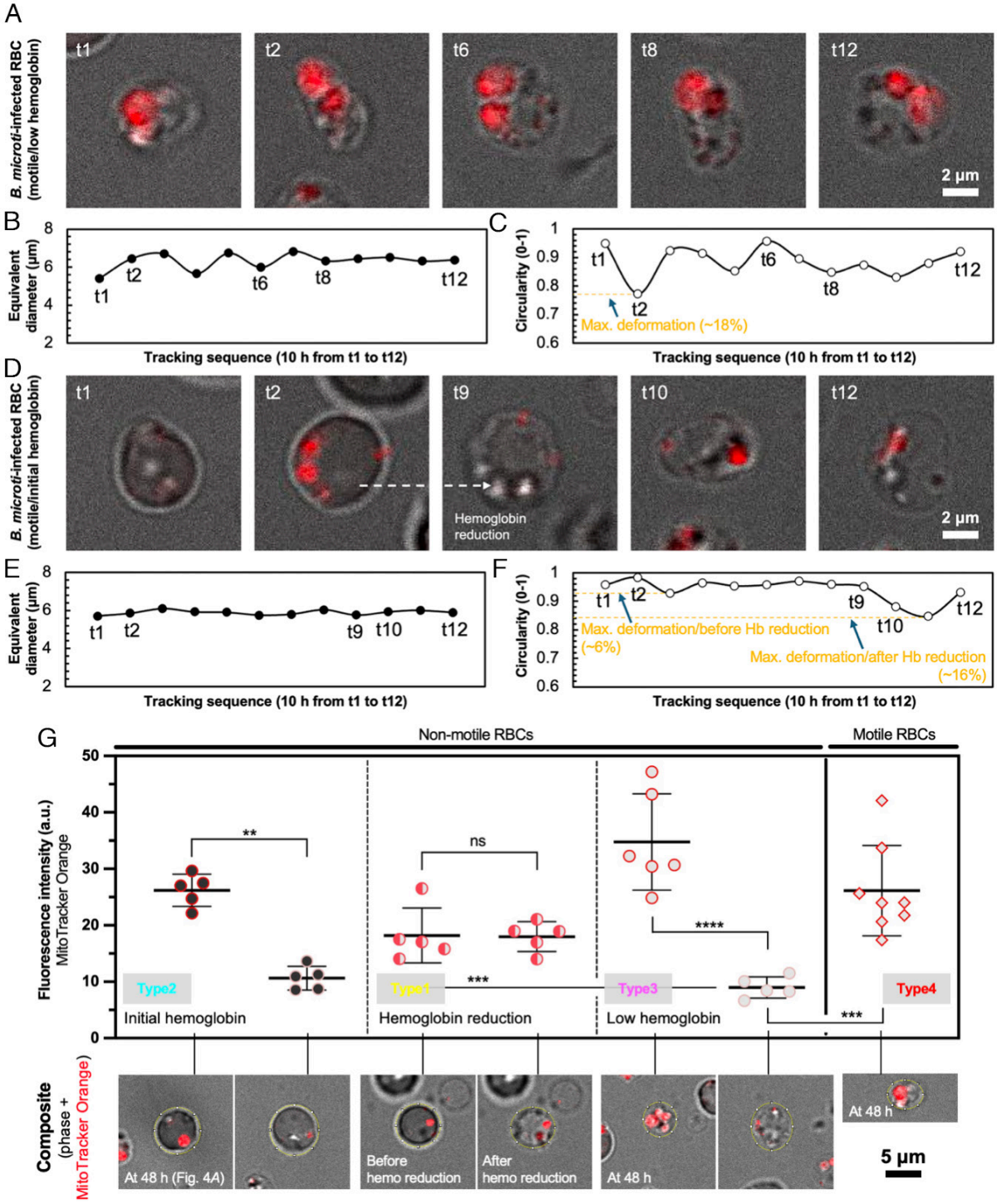

Fig. 6. Deformability and mitochondrial activity of the motile *B. microti*–infected RBCs. (*A*) Microscopic images (phase contrast + MitoTracker Orange) showing the deformation of a *B. microti*–infected RBC with low hemoglobin with the selected time points (t1 to t12) through the 10-h timelapse (Fig. 4*F*). (*B*) Cell size (equivalent diameter assuming circular cell shape) and (*C*) cell deformability (circularity 0—least circular, 1—perfectly circular). (*D*–*F*) Cell size and cell deformability results of *B. microti*–infected RBC with initial hemoglobin (Fig. 4*I*). (*G*) Mitochondrial activity of *B. microti* analysis probed by MitoTracker Orange fluorescence intensity corresponding to the cell types in Fig. 4*B*. MitoTracker Orange was stable against high-frequency laser scan, showing no noticeable photobleaching against 2% max. laser power (Leica, Stellaris 5, WLL) and 360 scans through 6 h (28). The RBCs in this mitochondrial activity analysis were based on the 10-h timelapse shown in Fig. 4 *A*–*C*. The subgroup of nonmotile RBCs experiencing hemoglobin reduction (Fig. 4*B*, Type 1) was analyzed, showing no change in mitochondrial activity before and after hemoglobin reduction (Fig. 4*C*). The subgroups of nonmotile RBCs with initially high hemoglobin (Fig. 4*B*, Type 2) and low hemoglobin (Fig. 4*B*, Type 3) did not show noticeable changes in hemoglobin levels during the timelapse. However, the Mitotracker fluorescence intensity diminished over time, which is reflected by two subgroups with high and low mitochondrial activity; representative images corresponding to these states, acquired across the timelapse, are presented. The subgroup of motile RBCs was analyzed in the first frame at 48 h in the timelapse (Fig. 4*A*). RBCs having the initial hemoglobin and low hemoglobin were grouped together (Fig. 4*B*, Type 4) to assess the overall mitochondrial activity associated with the acquired RBC motility. Also, a representative microscopic image (phase contrast + MitoTracker Orange) with high or low mitochondrial activity is shown. Each dot in Fig. 6*G* represents an RBC. Error bars, mean ± SD. A one-way ANOVA for multiple comparisons was used to calculate the *p*-values followed by a post hoc Student's *t* test. $^{**}P \le 0.01$, $^{***}P \le 0.001$, $^{****}P \le 0.0001$, and ns—not significant.

while remaining inside the host cell—rather than exclusively as free merozoites—may contribute to immune evasion or facilitate more efficient propagation. Several benefits to the parasite from this acquired motility can be envisioned, for example, possible fitness cost advantage without egress (i.e., not requiring the expression of perforin-like protein 1 (PLP1)] (36) or molecules with similar function that compromise the cytoplasmic membrane of the infected host cell), cloaking themselves within the host cell membrane components against immune surveillance, etc. Further studies and clarification of the molecular mechanisms and biological functions of the acquired mobility of *B. microti*–infected RBCs may reveal intervention targets that selectively impair/inactivate the parasite cloaking ability and motility and therefore enhance host immune control and/or reduction of the side effects of antiparasitics (39) (e.g., atovaquone targeting on mitochondria, azithromycin/clindamycin targeting on protein synthesis, quinine targeting on heme metabolism and DNA processes) on host cells.

Materials and Methods

Confocal Microscopy. The imaging of μ-Blood was performed on a Leica STELLARIS 5 confocal microscope. The objectives used in this study include HC PL APO CS2 20×/0.75 DRY [working distance (WD, 0.62 mm)], HC FLUOTAR L VISIR APO CS2 25×/0.95 WATER (WD, 2.40 mm), and HC PL APO CS2 63×/1.40 OIL (WD, 0.14 mm). The pinhole was set to 1 airy unit (AU) for all imaging. The OKOLab onstage incubator was used to control the cell culture environment on the microscope for 37 °C ambient air. MitoTracker Orange CMTMRos (2252, Lumiprobe) is a hydrophobic, membrane-permeable, cationic dye that stains the inner membrane of live mitochondria. Dead mitochondria lose the fluorescence of MitoTracker Orange over time due to the diminished inner membrane potential.

RBC Morphology Characterization. 1) RBC cytoplasmic membrane staining and confocal imaging. RBCs from uninfected and infected whole blood were stained with PKH67 green membrane stain (PKH67 Green Fluorescent Cell Linker Midi Kit for General Cell Membrane Labeling, Sigma Aldrich, excitation max: 490 nm/emission max: 502 nm) at a concentration of 4.45 μM, incubated at room temperature for 5 min, then washed once with fetal bovine serum (FBS) with centrifugation at 1,000× g for 5 min. Uninfected and infected RBCs were prepared for imaging by aliquoting 5 μL of the cell pellet onto a glass slide with a coverslip, or by loading 20 μL into a μ-Blood device following the previously described methods. Samples were imaged using the Leica STELLARIS 5 confocal microscope with HC PL APO CS2 63×/1.40 OIL objective. Z-stack step sizes were imaged at increments of 0.1 μm. 2) TEM. The RBC samples were fixed in cold 2.5% glutaraldehyde in 1× PBS. Samples were rinsed in PBS, postfixed in 1% osmium tetroxide with 1% potassium ferricyanide, rinsed in PBS, dehydrated through a graded series of ethanol and propylene oxide and embedded in Poly/Bed 812 (Glauert formulations). Semithin (300 nm) sections were cut on a Leica Reichart Ultracut, stained with 0.5% Toluidine Blue in 1% sodium borate and examined under the light microscope. Ultrathin sections (65 nm) were stained with uranyl acetate and Reynold's lead citrate and examined on JEOL 1400 Plus transmission electron microscope at 80 kV. 3) SEM. The RBC samples were fixed overnight in 2.5% glutaraldehyde in 1× PBS at 4 °C. Samples were washed three times in PBS, postfixed in aqueous 1% osmium tetroxide, and then washed three times in PBS. Samples were dehydrated through a graded ethanol series (30 to 90%), further dehydrated with absolute ethanol (100%). The samples were dehydrated further in hexamethyldisilazane (HMDS) and then removed to air dry. Samples were then mounted onto aluminum stubs, grounded with silver paint, and sputter coated with 3.5 nm gold/palladium (Cressington Sputter Coater Auto 108, Cressington, Watford, UK). Samples were viewed in a JEOL JSM-IT710 HRLV scanning electron microscope at 3 kV. 4) Hemoglobin concentration assay. Hemoglobin concentration of *B. microti*–infected RBCs and (control) uninfected RBCs from SCID mice were determined using Cayman's Hemoglobin Colorimetric Assay Kit and provided standard protocols from the manufacturer (Cayman Chemical, 700540). Whole blood samples (one uninfected, one infected, 100 μL per sample) were centrifuged at 1,000× g for 10 min at 4 °C. The plasma and buffy coat layers were carefully aspirated, and RBCs were collected from the pellet and stored briefly on ice until assaying. The RBC pellets from both samples were diluted 1:10 with the assay buffer before analyzing in technical triplicates. The absorbance at 575 nm was read on a plate reader (Agilent technologies, Cytation 5 Imaging Reader) and analyzed in comparison to the hemoglobin standard using DataGraph.

Image Analysis. Image analyses were completed in Fiji ImageJ as follows i) Cell count was performed using "Plugins–Analyze–Cell Counter." ii) Signal (e.g., grayscale, fluorescence) intensity and morphology (including size and shape) analyses were performed using "Analyze–Measure." "Set Measurements" for intensity analysis included "Mean gray value, SD, and Min & max gray value". Set Measurements for morphology analysis included "Shape descriptors and Feret's diameter." The region of interest (ROI) was defined using the shape selection tools on the objects of interest. iii) Motion tracking was performed using "Plugins–Tracking–Manual Tracking." In "Parameters," the time interval and x/y calibration (i.e., pixel size) were specified according to the setting of the timelapse videos. Tracking path images were saved using screenshots. The tracking trajectories were exported and saved in .csv. MSD and motion type analyses were executed in MATLAB using the standard MSD calculation algorithm (40). It is worth noting that α (i.e., the fitting exponent) in conventional MSD analysis (i.e., stochastic particle diffusion) only takes non-negative values (i.e., $\alpha \geq 0$, if $\alpha = 0$ it indicates the object stops moving). However, in biological systems and specifically tracking of the active movement of living cellular objects, α may take negative values (i.e., $\alpha < 0$) as reflected on an MSD plot with a decrease in MSD. A positive α indicates a movement of the object away from the tracking origin. In comparison, a negative α corresponds to a movement of the object toward the tracking origin. The α values shown in the paper were calculated with monotonic (i.e., continuously increasing or decreasing) segments of a trajectory. The α values of decreasing segments were displayed in absolute as $|\alpha|$. Supporting movies were edited in DaVinci Resolve 19 and Apple iMovie.

Data Visualization and Statistical Analysis. Raw data were directly used in statistical analysis with no data excluded. Data were averaged from at least 3 replicates and presented as mean ± SD if applicable. Data plotting and visualization were performed using GraphPad Prism (Ver. 10.4.1), Microsoft Excel, and Microsoft PowerPoint. All statistical analyses were performed using the *t* test (for paired data) or one-way ANOVA (for comparison of multiple data) followed by a post hoc Student's *t* test.

Data, Materials, and Software Availability. All data and code required to reproduce the analyses have been deposited at https://doi.org/10.1184/R1/30191635 (38).

ACKNOWLEDGMENTS. This work was supported by the National Institute of General Medical Sciences of the United States NIH, Grant No. 7DP2GM149553-02, and the NSF Graduate Research Fellowship Program, Grant No. DGE2140739. Any opinions, findings, and conclusions or recommendations expressed in this material are those of the authors and do not necessarily reflect the views of the NSF. We would like to thank the University of Pittsburgh's Center for Biologic Imaging for providing training and access to the JEOL JSM-IT710 HRLV scanning electron microscope, Grant No. S10OD036205-01 NIH for Simon Watkins, and JEOL 1400 Plus transmission electron microscope, Grant No. 1S10RR016236-01 NIH for Simon Watkins. We thank Emily Bache for assistance in collecting blood samples from mice.

1. C. A. Lobo, M. Singh, M. Rodriguez, Human babesiosis: Recent advances and future challenges. *Curr. Opin. Hematol.* **27**, 399–405 (2020).
2. E. G. Vannier, M. A. Diuk-Wasser, C. Ben Mamoun, P. J. Krause, Babesiosis. *Infect. Dis. Clin. North Am.* **29**, 357–370 (2015).
3. M. Swanson, A. Pickrel, J. Williamson, S. Montgomery, Trends in reported babesiosis cases–United States, 2011–2019. *Am. J. Transplant.* **23**, 582–584 (2023).
4. A. Hildebrandt, J. S. Gray, K.-P. Hunfeld, Human babesiosis in Europe: What clinicians need to know. *Infection* **41**, 1057–1072 (2013).
5. S. J. Drews *et al.*, Transfusion-transmitted spp.: A changing landscape of epidemiology, regulation, and risk mitigation. *J. Clin. Microbiol.* **61**, e0126822 (2023).
6. H. M. Heller, Babesiosis in immunosuppressed hosts: Pathogenesis, diagnosis and management. *Curr. Opin. Infect. Dis.* **37**, 327–332 (2024).

7. D. M. Tufts, M. A. Diuk-Wasser, Vertical transmission: A vector-independent transmission pathway of Babesia microti in the natural reservoir host *Peromyscus leucopus*. *J. Infect. Dis.* **223**, 1787–1795 (2021).
8. J. T. Joseph *et al.*, Vertical transmission of Babesia microti, United States. *Emerg. Infect. Dis.* **18**, 1318–1321 (2012).
9. K. Saetre *et al.*, Congenital babesiosis after maternal infection with Borrelia burgdorferi and *Babesia microti*. *J. Pediatr. Infect. Dis. Soc.* **7**, e1–e5 (2018).
10. B. Abittan *et al.*, A case of babesiosis in a pregnant patient treated with red blood cell exchange transfusion. *Case Rep. Obstet. Gynecol.* **2019**, 9869323 (2019).
11. A. Kumar, J. O'Bryan, P. J. Krause, The global emergence of human babesiosis. *Pathogens* **10**, 1447 (2021).
12. L. Schnittger, A. E. Rodriguez, M. Florin-Christensen, D. A. Morrison, Babesia: A world emerging. *Infect. Genet. Evol.* **12**, 1788–1809 (2012).
13. H. Hakimi, J. Yamagishi, S.-I. Kawazu, M. Asada, Advances in understanding red blood cell modifications by *Babesia*. *PLoS Pathog.* **18**, e1010770 (2022).
14. J. Thekkiniath *et al.*, Evidence for vesicle-mediated antigen export by the human pathogen. *Life Sci Alliance* **2**, e201900382 (2019).
15. B. Tuvshintulga *et al.*, Disruption of a DNA fragment that encodes the microneme adhesive repeat domain-containing region of the BBOV_III011730 does not affect the blood stage growth of Babesia bovis in vitro. *Mol. Biochem. Parasitol.* **255**, 111576 (2023).
16. R. G. Bastos *et al.*, Immunoreactive rhoptry-associated protein-1 paralogs are ancestral members of the piroplasmid-confined RAP-1 family. *Pathogens* **10**, 1384 (2021).
17. M. Asada *et al.*, Gliding motility of Babesia bovis merozoites visualized by time-lapse video microscopy. *PLoS One* **7**, e35227 (2012).
18. L. F. Westblade, M. S. Simon, B. A. Mathison, L. A. Kirkman, Babesia microti: From mice to ticks to an increasing number of highly susceptible humans. *J. Clin. Microbiol.* **55**, 2903–2912 (2017).
19. A. Puri *et al.*, Pathogen genomics, genetic variability, immunodominant antigens, and pathogenesis. *Front. Microbiol.* **12**, 697669 (2021).
20. E. Sevilla, L. M. González, D. Luque, J. Gray, E. Montero, Kinetics of the invasion and egress processes of Babesia divergens, observed by time-lapse video microscopy. *Sci. Rep.* **8**, 14116 (2018).
21. V. Djokic, L. Akoolo, N. Parveen, Infection changes host spleen architecture and is cleared by a Th1 immune response. *Front. Microbiol.* **9**, 85 (2018).
22. A. J. Zimmer, K. A. Simonsen, *Babesiosis* (StatPearls Publishing, Treasure Island, FL, 2023).
23. I. Borggraefe *et al.*, Babesia microti primarily invades mature erythrocytes in mice. *Infect. Immun.* **74**, 3204–3212 (2006).
24. C. M. Elton, M. Rodriguez, C. Ben Mamoun, C. A. Lobo, G. J. Wright, A library of recombinant Babesia microti cell surface and secreted proteins for diagnostics discovery and reverse vaccinology. *Int. J. Parasitol.* **49**, 115–125 (2019).
25. R. Magni, A. Luchini, L. Liotta, R. E. Molestina, Analysis of the Babesia microti proteome in infected red blood cells by a combination of nanotechnology and mass spectrometry. *Int. J. Parasitol.* **49**, 139–144 (2019).
26. H. Gong, L. He, H. F. Alzan, Editorial: Exploring new technologies, investigating new targets, and shedding new light on. *Front. Cell. Infect. Microbiol.* **12**, 1004875 (2022).
27. C. Li *et al.*, Microliter whole blood neutrophil assay preserving physiological lifespan and functional heterogeneity. *Small Methods* **8**, e2400373 (2024).
28. C. Li, E. G. Bache, A. L. Apgar, D. M. Tufts, T. H. R. Niepa, In vitro monitoring of babesia microti infection dynamics in whole blood microenvironments. *Adv. Sci. (Weinh)* **12**, e08185 (2025).
29. F. Barros-Becker, P.-Y. Lam, R. Fisher, A. Huttenlocher, Live imaging reveals distinct modes of neutrophil and macrophage migration within interstitial tissues. *J. Cell Sci.* **130**, 3801–3808 (2017).
30. A. D'Alessandro *et al.*, Red blood cell metabolism in vivo and in vitro. *Metabolites* **13**, 793 (2023).
31. S. Shikano *et al.*, Mitochondrial function in Babesia microti and *Babesia rodhaini*. *Int. J. Parasitol.* **28**, 567–570 (1998).
32. M. M. Gozar, W. J. O'Sullivan, A. S. Bagnara, Mitochondrial function in *Babesia bovis*. *Int. J. Parasitol.* **22**, 165–171 (1992).
33. M. C. Ulucesme, M. Aktas, S. Ozubek, Mitochondrial genome analysis of (Apicomplexa: Babesiidae) endemic in sheep in Türkiye. *Vet. Sci.* **11**, 554 (2024).
34. B. Cunniff, A. J. McKenzie, N. H. Heintz, A. K. Howe, AMPK activity regulates trafficking of mitochondria to the leading edge during cell migration and matrix invasion. *Mol. Biol. Cell* **27**, 2662–2674 (2016).
35. C. Li *et al.*, Social motility of biofilm-like microcolonies in a gliding bacterium. *Nat. Commun.* **12**, 5700 (2021).
36. M. S. Paoletta *et al.*, The key to egress? <i>Babesia bovis perforin-like protein 1 (PLP1) with hemolytic capacity is required for blood stage replication and is involved in the exit of the parasite from the host cell. *Int. J. Parasitol.* **51**, 643–658 (2021).
37. J. H. Schrope *et al.*, Confinement by liquid-liquid interface replicates in vivo neutrophil deformations and elicits bleb-based migration. *Adv. Sci.* **12**, e2414024 (2025).
38. C. Li, A. L. Apgar, D. M. Tufts, T. H. R. Niepa, Dataset for acquired motility of Babesia microti–infected red blood cells. Carnegie Mellon University. https://doi.org/10.1184/R1/30191635. Deposited 13 January 2026.
39. I. Renard, C. Ben Mamoun, Treatment of human babesiosis: Then and now. *Pathogens* **10**, 1120 (2021).
40. Y. Wang, Y. Jeong, S. M. Jhiang, L. Yu, C.-H. Menq, Quantitative characterization of cell behaviors through cell cycle progression via automated cell tracking. *PLoS One* **9**, e98762 (2014).